COMPUTER METHODS IN MATERIALS SCIENCE

2025, vol. 25, no. 3, 5–18
https://doi.org/10.7494/cmms.2025.3.1025

Polycrystalline plasticity analysis of cyclic loading and stress relaxation in 316H austenitic stainless steel

Sadik Sefa Acar, Tuncay Yalçinkaya*

Department of Aerospace Engineering, Middle East Technical University, Ankara, 06800, Turkiye.

Abstract

The mechanical behavior of 316H austenitic stainless steel is investigated in this study under cyclic strain-controlled loading with and without hold periods at elevated temperatures. Understanding the low-cycle fatigue (LCF) and fatigue-creep interaction (FCI) characteristics is essential for ensuring the structural performance and safety of reactor components, particularly under conditions typical of modular and generation IV reactors. The new generation of nuclear power plants require more resistant and durable materials as the operating environments impose significantly higher demands, including increased neutron irradiation levels and elevated operating temperatures, leading to accelerated material degradation. A combined isotropic-kinematic hardening model within a crystal plasticity framework is employed to capture the cyclic and time-dependent mechanical response of the material. Model parameters are calibrated by fitting cyclic loading simulation results to experimental data at 550°C using polycrystalline representative volume elements (RVE). Strain-controlled uniaxial loading simulations are performed to analyze peak stress evolution throughout cyclic loading and stress relaxation behavior during strain-hold periods. The RVE simulation results are in strong agreement with experiments under LCF loading. For the loading with strain-holds, stress relaxation during hold periods exhibits two distinct stages: an initial rapid decay followed by a steady decline, both of which are captured in simulations. Beyond the macroscopic response, analyses reveal the heterogeneous evolution of field variables at the microstructural level, as strain hardening during loading and stress relaxation during hold periods varied across grains due to their crystal orientations and interactions with neighboring grains. These findings enhance the understanding of high-temperature mechanical behavior at both macroscopic and microstructural scales, contributing to the efforts for the design, operation, and life extension of nuclear reactor components.

Keywords: stress relaxation, peak stress, strain hold, stainless steel, crystal plasticity, back-stress, DAMASK

1. Introduction

Materials used in nuclear plants undergo various mechanical and thermal loadings throughout their operational use. During both design and operation phases, ensuring the reliability and durability of these materials requires an understanding of material behavior. Material behavior is a complex synthesis of the external loading and the material properties, including microstructure. Therefore, an accurate estimation of the performance of materials in nuclear plants necessitates the identification of loading histories under service, the development and verification of tools for the assessment of the material behavior, and finally, the utilization of tools developed for the identified loading histories. These estimation efforts include the characterization of

* Corresponding author
Author's e-mails: sadik.acar@metu.edu.tr, yalcinka@metu.edu.tr
ORCID ID's: 0009-0003-1854-4823 (S. S. Acar), 0000-0002-7982-1105 (T. Yalçinkaya)
Received: 30.05.2025, accepted: 15.09.2025, published: 21.11.2025

the material behavior under cyclic and time-dependent mechanical loadings at elevated temperatures.

One of the materials used in nuclear plants is the 316H austenitic stainless steel, for which knowledge of its fatigue and creep performance is of high importance due to ongoing nuclear plant life extension projects, along with new plant projects. 316H austenitic stainless steels are widely used in European nuclear plants such as Advanced Gas-cooled Reactor (AGR) in the UK (Gredis, 2022; Nasser et al., 2016) and also in other nuclear plants such as Sodium-cooled Fast Reactor (SFR) in China (Du et al., 2023; Xu et al., 2022). The most common operational conditions for 316H alloy in nuclear power plants involve service temperatures of 550°C for both AGRs (Petkov et al., 2021) and SFRs (Xu et al., 2021). The operational condition of an AGR boiler made of 316H can be idealized as uniaxial strain-controlled cyclic loading at 550°C, strain-hold dwells at peak strain (Hughes et al., 2019; Petkov et al., 2019).

Under cyclic loading at elevated temperatures, metallic material undergoes a combination of fatigue and creep deformation mechanisms. Strain-controlled Low Cycle Fatigue (LCF) loading leads to a progressive increase in the plastic deformation and degradation of the material. LCF loading may lead to cyclic hardening (Pan et al., 2022) or cyclic softening (Zhao & Chen, 2020) of the metallic material, depending on the material properties and the loading conditions, particularly the temperature and the hold time. Cyclic hardening of the material under LCF loading occurs due to the progressive accumulation of dislocations and the retardation of dislocation motion. At 550°C, the microstructural evolution in 316H during deformation strongly depends on the strain amplitude of the cyclic loading. Xu et al. (2021) showed that, at lower amplitudes (±0.3%), dislocations rearrange into planar wall structures that often accumulate parallel to grain boundaries. For a higher strain amplitude (±0.3%), wall structures intersect grain boundaries, and imperfectly developed cells start to appear. At the strain amplitude of ±0.5%, well-developed dislocation cells with accompanying walls with high density dislocation tangles dominate within grains. For 316H, time-dependent static recovery and rate-dependent dynamic recovery processes contribute to the saturation of the maximum stress after a number of cycles during cyclic loading at 550°C (Phan et al., 2019). At this temperature, cyclic softening, identified by the decrease in maximum stress, may be observed as a result of the promoted fatigue-creep interaction (FCI) mechanisms due to strain-hold dwells (Zhao & Chen, 2020). For 316H at 550°C, during strain-hold dwells, the spacing of dislocation junctions increases due to thermal recovery, which reduces obstacles to glide, and produces a softening of the subsequent hysteresis loop. In addition, prior cyclic hardening lowers both the primary creep strain and the minimum creep rate measured in a following strain-hold dwell, due to the strengthened dislocation network. The balance between hardening and thermal recovery during strain-hold dwell is obtained earlier for a denser dislocation network (Petkov et al., 2021).

Stress relaxation is a time-dependent phenomenon describing the reduction in the macroscopic stress during strain-controlled hold periods. As the total strain is kept constant, creep mechanisms eventually lead to an increase in creep strain and a decrease in the elastic strain. Creep strain is accumulated within the material as the diffusion, dislocation climb, and grain boundary sliding govern the creep deformation at elevated temperatures. By modifying the dislocation structure and affecting other creep mechanisms such as dislocation climb and cross-slip, recovery processes are among the factors determining the stress relaxation (Karjalainen & Perttula, 1996). Through recovery processes, immobile and mobile dislocations generated by prior plastic deformation are annihilated, and a balancing effect is introduced to the strain hardening. Activation and relative domination of these mechanisms depend on the material, the temperature, the loading condition, and the stage of the creep. Coules et al. (2022) experimentally observed that a very significant amount of stress relaxation occurs during long strain holds up to 800 h for 316H at 550°C. Du et al. (2023) found that for the same material and temperature, stress relaxation still occurs even during much shorter hold durations of cyclic loading with 3-minute hold periods. Wang H. et al. (2013) measured the evolution of the lattice strains during stress relaxation of 316L. They found that, in the first stage of the relaxation, the stress drops rapidly, and lattice strains sharply decrease, which suggests that this stage is dominated by the rate-dependent thermally-activated glide mechanisms. After the first stage, stress decreases asymptotically while creep strains accumulate and the lattice strains remain unmodified, pointing out the time-dependent nature of the latter stage of stress relaxation in stainless steels. Additionally, Hormozi et al. (2015) showed that the percentage of stress reduction in the first stage of the relaxation is higher for greater total strain values at elevated temperatures. This observation proves the transition from glide-governed processes to diffusion-governed and grain boundary sliding-governed processes during relaxation, since higher initial total strain results in increased mobile dislocation activity during the initial stage of the relaxation.

Assessment of material behavior under cyclic loading and stress relaxation using empirical methods is costly and time-consuming, particularly at elevated temperatures. To provide methodology and standardize the designing and building of mechanical components used in SFR nuclear plants, the RCC-MR code has been developed. RCC-MR code provides the high-temperature mechanical assessment approaches for nuclear materials, including 316 stainless steel (AFCEN, 1985). Beyond the RCC-MR code, there have been many studies in the literature extending prior empirical approaches by developing computational methods supported by experimental data. Chen et al. (2011) employed primary and secondary constitutive forward creep (creep at constant stress) equations suggested in RCC-MR to describe the evolution of the creep strain and stress relaxation for 316H at 550°C. Wang Y. Q. et al. (2016) modified the RCC-MR forward creep model to predict the stress relaxation of 316H under constant-strain loading conditions. Hu C. & Cocks (2016) introduced a multi-scale self-consistent formulation for 316H in which each grain behaves as a spherical inclusion embedded in a homogeneous isotropic elastic medium, accounting for dislocation interactions and strengthening due to solute atoms. Petkov et al. (2019) extended the SCM model proposed by Hu C. & Cocks (2016) by employing crystal plasticity (CP) modeling to capture the anisotropic response of each grain under cyclic loading and strain-hold conditions. Erinosho et al. (2018) modeled the cyclic response of 316H using a phenomenological power-law flow rule with slip resistance evolution containing a state variable accounting for softening due to dislocation climb. Hu J. et al. (2023) predicted the crack propagation behavior of 316H by coupling a damage evolution model with a combined isotropic-kinematic hardening cyclic constitutive model incorporating strain range memory effects without considering microstructural effects. Allen et al. (2025) predicted stress relaxation and multiaxial deformation of 316H at 550°C employing the crystal plasticity model given in Agius et al. (2020), which utilizes time-dependent and time-independent power-law components in the flow rule along with Armstrong–Fredrick type back-stress evolution equation.

The current study employs a combined isotropic-kinematic hardening CP model containing stress and strain memory terms to better represent the cyclic response of the 316H polycrystal at 550°C. The model parameters are calibrated using experimental cyclic hysteresis loops using a polycrystal generated within a representative volume element (RVE). Simulation results for peak stress evolution under cyclic loading and stress relaxation under strain-hold conditions are compared to their experimental counterparts at different cycle numbers. Additionally, stress and strain distributions within the polycrystal are examined. Many numerical studies are present in the literature on this subject, but they either did not follow a microstructure-sensitive approach and assess only the macroscopic response or utilized a crystal plasticity model that does not combine isotropic and kinematic hardening or include memory terms. Building upon the existing literature, the study aims to assess the evolution of material behavior of 316H under cyclic loading and strain-hold periods from a microstructural perspective.

2. Theory

In this study, the combined isotropic-kinematic hardening (IK) model is utilized within the DAMASK crystal plasticity framework. The IK model, originally developed by Wollmershauser et al. (2012) for small strain deformation, has already been implemented in the DAMASK with finite strain framework (Roters et al., 2019). This framework employs a multiplicative decomposition of the total deformation gradient $\mathbf{F}$ into elastic $\mathbf{F}_e$ and plastic components $\mathbf{F}_p$:

$$\mathbf{F} = \mathbf{F}_e \mathbf{F}_p \tag{1}$$

To obtain the stress tensor at each material point using the elastic deformation gradient, firstly, the plastic deformation gradient has to be calculated. The solution of the below relation, formulated implicitly, yields the plastic deformation gradient at the current configuration.

$$\frac{\mathbf{F}_p(t) - \mathbf{F}_p(t_0)}{\Delta t} = \mathbf{L}_p(t)\mathbf{F}_p(t) \tag{2}$$

At any time point, the plastic velocity gradient $\mathbf{L}_p$ is calculated by summing the slip rate contributions of each slip system α as:

$$\mathbf{L}_p = \sum_{\alpha} \dot{\gamma}^{\alpha} (\mathbf{m}^{\alpha} \otimes \mathbf{n}^{\alpha}) \tag{3}$$

In the formulation of the plastic velocity gradient, $\mathbf{m}^{\alpha}$ and $\mathbf{n}^{\alpha}$ denote the slip direction and slip plane normal unit vectors of slip system α, respectively. Slip rate is represented by $\dot{\gamma}^{\alpha}$ and evolves according to the below flow rule:

$$\dot{\gamma}^{\alpha} = \dot{\gamma}_0{}^{\alpha} \left(\frac{\tau^{\alpha} - \tau_{bs}{}^{\alpha}}{\tau_{for}{}^{\alpha}} \right)^n \tag{4}$$

Here, $\dot{\gamma}_0$ represents the reference slip rate, and n is the rate sensitivity exponent. Effective shear stress on a slip system is found by subtracting the back-stress $\tau_{bs}{}^{\alpha}$

from the resolved shear stress τ^{α}. Forest stress is denoted by $\tau_{for}{}^{\alpha}$. Resolved shear stress acting on a slip system is a function of the second Piola–Kirchhoff stress **S**, and slip direction $\mathbf{m}^{\alpha}$ and slip plane normal $\mathbf{n}^{\alpha}$ vectors of that slip system defined in the global coordinate system as:

$$\tau^{\alpha} = \mathbf{S}: (\boldsymbol{m}^{\alpha} \otimes \boldsymbol{n}^{\alpha}) \tag{5}$$

Evolutions of forest stress and back-stress are governed by corresponding hardening formulations, which provide isotropic and kinematic hardening effects, respectively. The rate of forest stress and corresponding self-hardening modulus is formulated as:

$$\dot{\tau}_{for}{}^{\alpha} = \sum_{\beta} q^{\alpha\beta} h_{for}^{\alpha\alpha} \dot{\gamma}^{\beta} \tag{6}$$

$$h_{for}{}^{\alpha\alpha} = h_{1,for} + \left(h_{0,for} - h_{1,for} + \Gamma \left(\frac{h_{0,for} h_{1,for}}{\tau_{1,for}} \right) \right) e^{-\Gamma \left(\frac{h_{0,for}}{\tau_{1,for}} \right)} \tag{7}$$

where the ratio of latent hardening to self-hardening $q^{\alpha\beta}$ is set to 1 for all slip system interactions. This simplification was adopted because no experimental latent-hardening data could be found for 316H at 550°C in the literature. Self-hardening modulus for isotropic hardening is represented by $h_{for}{}^{\alpha\alpha}$, and its value is determined by material parameters, initial forest hardening modulus $h_{0,for}$, saturation forest hardening modulus $h_{1,for}$, and saturation forest slip resistance $\tau^{1,for}$ along with total accumulated slip Γ, accounting for the amount of slip across all slip systems. Kinematic hardening is formulated as:

$$\dot{\tau}_{bs}{}^{\alpha} = \sum_{\beta} q^{\alpha\beta} h_{bs}^{\alpha\alpha} \dot{\gamma}^{\beta} \tag{8}$$

$$h_{bs}{}^{\alpha\alpha} = h_{1,bs} + \left(h_{0,bs} - h_{1,bs} + \left(\gamma^{\alpha} - \gamma_0{}^{\alpha} \right) \left(\frac{h_{0,bs} h_{1,bs}}{\tau_{1,bs} + \chi_0{}^{\alpha}} \right) \right) \cdot e^{-\left(\gamma^{\alpha} - \gamma_0{}^{\alpha} \right) \left(\frac{h_{0,bs}}{\tau_{1,bs} + \chi_0{}^{\alpha}} \right)} \tag{9}$$

For the rate of back-stress and corresponding self-hardening modulus, the forest terms in the isotropic hardening formulation are replaced by their back-stress counterparts. Total accumulated slip Γ is replaced by $(\gamma^{\alpha} - \gamma_0{}^{\alpha})$ where γ^{α} refers to the amount of slip on an individual slip system and $\gamma_0{}^{\alpha}$ denotes the strain memory term accounting for the maximum amount of slip reached on that slip system before the last load reversal. Also, for the kinematic hardening formulation, saturation slip resistance is increased by the stress memory term $\chi_0{}^{\alpha}$ which refers to the maximum back-stress on a slip system reached before the last load reversal. After each load reversal, memory terms are updated to their new values. These memory terms are internal state variables and evolve throughout the simulation. They provide the remembering of the deformation history and a more accurate representation of material behavior under cyclic loading.

3. Numerical model

The DAMASK framework with its spectral solver and combined isotropic-kinematic hardening plasticity model is employed in this study. Crystal plasticity simulations are performed on a representative volume element (RVE) comprising 200 grains. RVEs are artificial microstructures exhibiting similar mechanical properties as the macroscopic body (Acar et al., 2022; Aydiner et al., 2024; Yalçinkaya et al., 2021). RVEs enable the assessment of various microstructural properties under desired loading conditions with much smaller computational time compared to larger models. Also, crystal plasticity analyses employing RVEs incorporate material properties at the grain-scale and produce local outputs that allow for the capturing of variations in mechanical response across the microstructure (Tatli & Yalçinkaya, 2025). In this study, the RVE generation process is comprised of two steps: the generation of a microstructure model through the Voronoi tessellation method and transformation of the model to a grid-type regular raster tessellation (Quey et al., 2011). The first step starts with the initial random guess of the grain positions as seed points. Then, the Voronoi tessellation method is employed while a three-dimensional morphology is generated based on seed points filling the RVE. A residual value is calculated at the first increment based on the defined convergence criteria across the whole domain. The only convergence criterion defined in this study is that the diameter of each grain has to be close to one another with a small allowance. In the second increment, seed points are moved to the volumetric centroids of grains. Then, the morphology is updated by the reconstruction of grain interfaces, altering morphology. At each increment, seed points are moved to new centroids, and grain interfaces are reconstructed such that the residual value for the convergence is minimized. At the end of the first step of RVE generation, the microstructure consists of 200 grains with a convex shape and similar diameters. In the second step, the RVE is discretized using a grid-type regular mesh containing 8000 points since the spectral solver requires the discretization of the body into regularly and equally spaced Fourier Points. A previous study conducted by

the authors showed that for the 304L alloy, employing an RVE with 200 grains discretized into 8000 points eliminates statistical scattering effects associated with RVE size and grid resolution (Acar & Yalçinkaya, 2025a). The generated RVE and grid mesh are illustrated in Figure 1. Voxels constituting the solution domain have identical volumes. Since voxels continue to have identical volumes throughout the simulation, contributions of the solution for each grid point to the field variable results have the same weight. Therefore, homogenization to obtain macroscopic quantities is carried out by simply averaging field variables during post-processing.

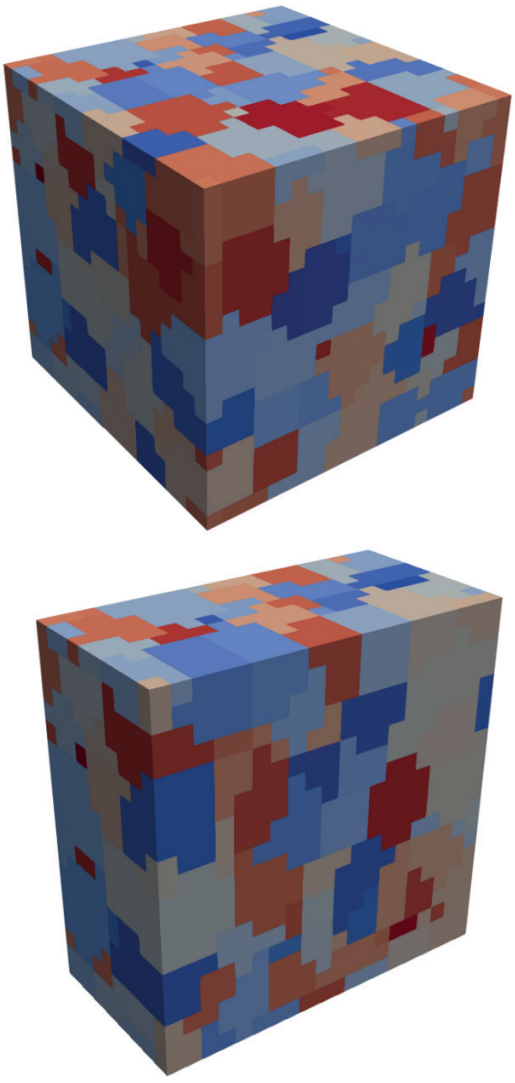

Fig. 1. Representative volume element containing 200 grains discretized into raster tesselation

The spectral method based on Fast Fourier Transform (FFT) in the DAMASK framework is used throughout the crystal plasticity simulations. The spectral solver uses the so-called "basic scheme" derived from the direct variational formulation to solve the mechanical equilibrium in the Fourier space (Eisenlohr et al., 2013; Shanthraj et al., 2015). The comparison between the finite element method (FEM) and the spectral solver has been made in several studies, showing the spectral solver produces similar results to FEM (Geus et al., 2017). Furthermore, the FEM solver requires nearly two times the computational time needed by the spectral solver (Acar & Yalçinkaya, 2025b). Roters et al. (2012) showed that the spectral solver necessitates less memory than FEM.

For both monotonic and cyclic strain-controlled loading simulations, boundary conditions are prescribed by the manipulation of the average deformation gradient tensor ($\bar{\mathbf{F}}$) and the average First Piola–Kirchhoff stress tensor ($\bar{\mathbf{P}}$) at each time increment. For the strain boundary condition, the axial normal direction along the x-axis is chosen as the loading direction, and the corresponding term in the average deformation gradient tensor ($\bar{F}_{11}$) is manipulated at each time increment to prescribe the desired loading shape. The average deformation gradients in normal directions, excluding the loading direction, are left unconstrained. All the shear terms in $\bar{\mathbf{F}}$ are set to be constrained. For the stress boundary condition, the average stress values in normal directions, excluding the loading direction, are constrained. The rest of the terms in $\bar{\mathbf{P}}$ tensor are left unconstrained. The boundary conditions are given below, where the asterisk (*) sign denotes unconstrained terms.

$$\bar{\mathbf{F}} = \begin{bmatrix} \bar{F}_{11} & 0 & 0 \\ 0 & * & 0 \\ 0 & 0 & * \end{bmatrix}, \quad \bar{\mathbf{P}} = \begin{bmatrix} * & * & * \\ * & 0 & * \\ * & * & 0 \end{bmatrix} \tag{10}$$

For monotonic strain-controlled loading, $\bar{F}_{11}$ is gradually increased to 1.1 in 100 s to impose 10% engineering strain. The uniaxial cyclic loading is achieved by enforcing a triangular and trapezoidal waveform on $\bar{F}_{11}$ for the loading without and with hold periods, respectively. For cyclic loading without hold periods, the mean strain (ε_{mean}) varies between 0% and 0.4% while the maximum strain (ε_{mean}) is kept constant at 0.5%. The uniaxial cyclic loading with hold periods incorporates a 3-minute strain-hold duration occurring at the tensile peak of each cycle. The strain rate is kept constant at $10^{-3}s^{-1}$ during both loading and unloading phases. Loading parameters, including strain amplitude (ε_{amp}), minimum strain (ε_{min}), mean strain (ε_{mean}), maximum strain (ε_{max}), strain ratio (R_{ε}), and cyclic hold duration (t_{hold}) are presented in Table 1. The loading conditions are illustrated in Figure 2.

Table 1. Loading parameters used in cyclic loading simulations

Type	ε_{amp} [%]	ε_{min} [%]	ε_{mean} [%]	ε_{max} [%]	R_{ε}	t_{hold} [s]
CL	0.5	–0.5	0.0	0.5	–1.0	0.0
CL	0.4	–0.3	0.1	0.5	–0.6	0.0
CL	0.3	–0.1	0.2	0.5	–0.2	0.0
CL	0.2	0.1	0.3	0.5	0.2	0.0
CL	0.1	0.3	0.4	0.5	0.6	0.0
CLH	0.5	–0.5	0.0	0.5	–1.0	180.0

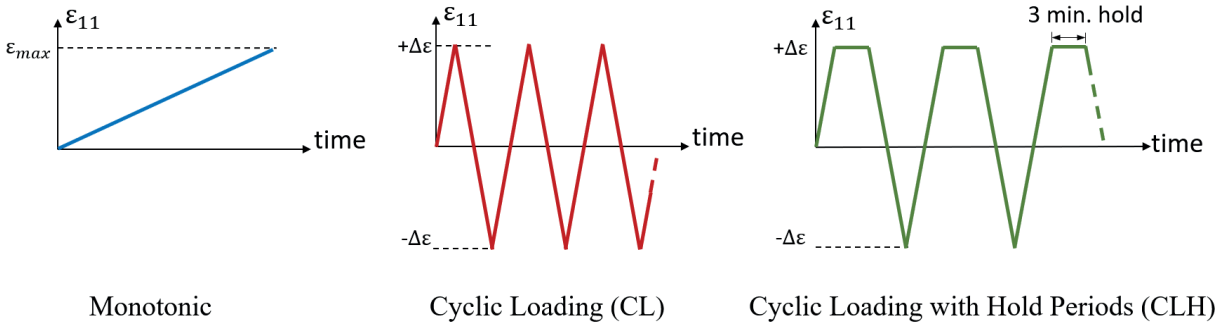

Fig. 2. Illustration of loading conditions as a time history of axial strain in corresponding simulations

The simulations in this study are conducted isothermally at 550°C. Accordingly, all material parameters are treated as constants. No explicit temperature-dependence is included, since the simulated conditions involve a constant elevated temperature. The results and conclusions of this study are only valid for the isothermal loading case. Elastic constants for 316H austenitic stainless steel at 550°C are taken from work by Du et al. (2023) as E = 135 GPa and ν = 0.3. These values are transformed to cubic elastic constants as C_{11} = 181.7 GPa, C_{12} = 77.9 GPa, and C_{44} = 51.9 GPa. Crystal plasticity model parameters are calibrated by fitting simulation results to experimental data taken from publication by Du et al. (2023) for hysteresis loops under strain-controlled uniaxial cyclic loading. The experimental data is processed, and hysteresis loops for the 1st and the 200th cycles are extracted. In the work by Du et al. (2023), it was found that peak stress during a cycle saturates at about the 52nd cycle under strain-controlled cyclic loading. Also, experimental hysteresis loops become indistinguishable from one another after about the same number of cycles. Therefore, it was assumed that the experimental hysteresis loop for the 70th cycle is almost the same as that for the 200th cycle. For the parameter identification simulations, the crystal orientation of each grain within the RVE is assigned randomly. Then, a considerable number of CP parameter combinations are generated and assigned to grains. Similar to the reference experiment, parameter identification simulation is conducted by imposing a strain-controlled uniaxial symmetric cyclic loading with 0.5% strain amplitude for 70 cycles. Simulation results are post-processed, and the hysteresis loops for the 1st and the 70th cycles are extracted. Hysteresis loops obtained by simulations are compared against their experimental counterparts. Among numerous CP parameter combinations used in simulations, the parameter set providing the closest homogenized stress response to the experimental response is employed in the rest of the work. Figure 3 illustrates the comparison of the experiment results and simulation results conducted with fitted model parameters. CP model parameters are shown in Table 2.

Table 2. Combined isotropic-kinematic hardening model parameters calibrated for 316H austenitic stainless steel

$\tau_{0,for}$ [MPa]	$\tau_{s,for}$ [MPa]	$h_{0,for}$ [MPa]	$h_{s,for}$ [MPa]	$\tau_{s,bs}$ [MPa]	$h_{0,bs}$ [MPa]	$h_{s,bs}$ [MPa]	$\dot{\gamma}_0$	n
42	60	150	1	17	8000	600	0.0001	60

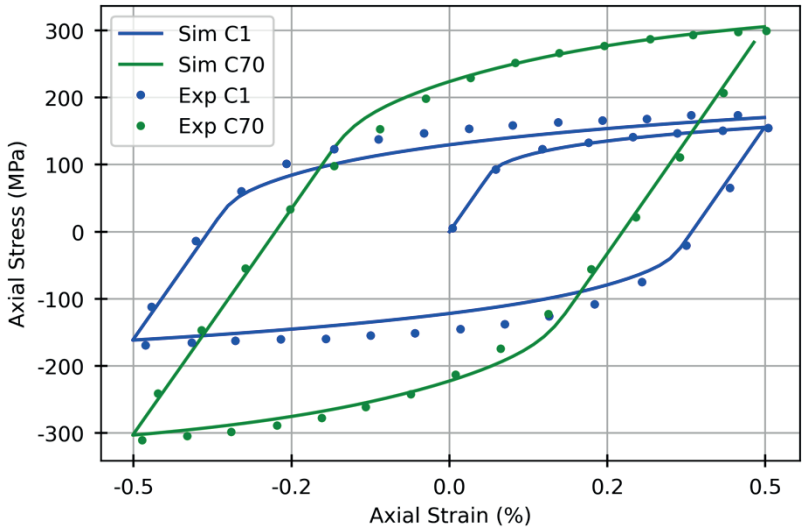

Fig. 3. Hysteresis loops for 1st and 70th cycles obtained by simulation using calibrated model parameter set and experiment taken from the work by Du et al. (2023), under symmetric cyclic loading with 0.5 % strain amplitude

The obtained parameter set is also used in monotonic loading simulations. The experimental uniaxial tensile loading results are compared to the simulation results in Figure 4. Even though model parameters are calibrated by using cyclic loading experiments, the same parameter set can also reproduce the macroscopic response of the material under monotonic loading. The agreement of up to 8% strain is consistent with the strain levels relevant to the cyclic and relaxation simulations in this study.

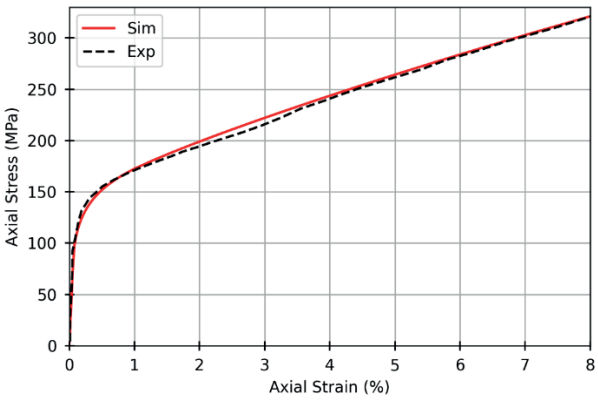

Fig. 4. Stress and strain results obtained by RVE simulation and experiment taken from work by Du et al. (2023) under uniaxial strain-controlled monotonic loading

4. Results

Firstly, the peak stress evolution of 316H austenitic stainless steel at 550°C under strain-controlled uniaxial cyclic loading is investigated using a combined isotropic–kinematic hardening crystal plasticity model. A symmetric cycling experiment with a 0.5% strain amplitude, conducted by Du et al. (2023), is used for comparison. The microstructural model generated within the RVE is subjected to uniaxial tension–compression loading with the same strain amplitude. The homogenized mechanical response of the RVE provides the macroscopic stress–strain behavior, from which the peak stress of each cycle is extracted and compared to the experimental data as illustrated in Figure 5. Peak stress is defined as the maximum stress within a given cycle. Simulation results show that the model accurately captures the experimentally observed peak stress evolution over all 70 cycles. Importantly, only the responses from the 1st and 70th cycles were used for parameter calibration, as the peak stresses of the intermediate cycles (2–69) were deliberately withheld and treated as an independent validation set. The close agreement achieved for these cycles demonstrates the model's capability to reproduce cyclic hardening behavior beyond the fitted data.

After assessing the macroscopic response, local microstructural variations in the mechanical behavior under cyclic loading are examined. As illustrated in Figure 5, the evolution of axial stress distributions at the peak of each cycle reveals that, with increasing cycle count, not only does the macroscopic peak stress reach saturation, but the stress distribution within the microstructure also stabilizes. Beyond a certain number of cycles, the distributions become nearly indistinguishable from one another, indicating that strain hardening reaches a steady configuration despite continued cyclic loading. Figure 6 presents axial true stress

and true strain contours at the peak of the final cycle within the RVE. At this point, the prescribed true strain is about 0.5% and the homogenized macroscopic true stress response is approximately 310 MPa. However, the contour plots reveal significant heterogeneity in local field variables. True stress values in the microstructure range from 157 MPa to 470 MPa, while true strain varies between 0.21% and 1.1%. These variations arise from the crystallographic anisotropy of the polycrystalline material. Grains with unfavorable orientations having low Schmid Factor (SF) resist slip and tend to sustain higher local stresses. These grains appear as stress hotspots in the contours. Conversely, grains with favorable orientations (high SF) have easier slip activation and thus accumulate a higher amount of strain while carrying relatively low stress. Additionally, mechanical compatibility requirements at grain boundaries induce further localization effects, as adjacent grains with differing orientations impose geometric constraints on one another.

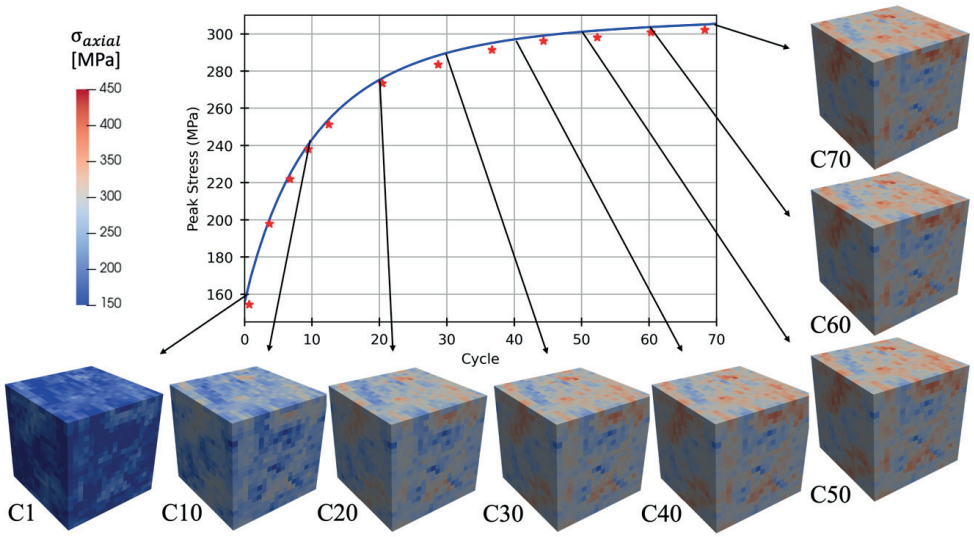

Fig. 5. Evolution of axial true stress distribution, and the peak stress curve obtained by simulation and experiment taken from work by Du et al. (2023) under symmetric loading with 0.5% strain amplitude.

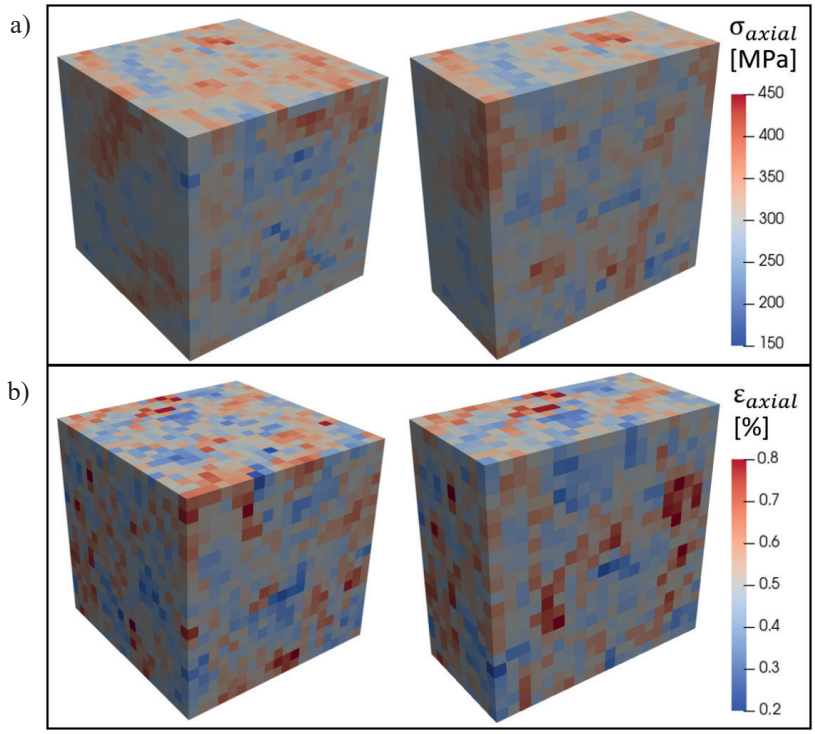

Fig. 6. Spatial distributions of (a) axial true stress and (b) axial true strain in the polycrystalline RVE at the peak of the 70th cycle under symmetric loading with a strain amplitude of 0.5%

After evaluating the response under symmetric loading, a series of simulations is conducted in which the mean strain (ε_m) varies from 0% to 0.4%, while the maximum strain remained fixed at 0.5%. Figure 7 compares the resulting hysteresis loops for cycles 1 and 70. Figure 8 illustrates the evolution of the peak axial stress, the average critical resolved shear stress (CRSS), and the average total plastic slip. To construct the CRSS curve, the CRSS values for all slip systems are first averaged at each material point and then homogenized over the microstructure domain. The total slip curve is obtained by summing slip values on all systems at each point, followed by spatial homogenization. Finally, CRSS and total slip evolutions are sampled at the peak of every cycle. Results show that the material undergoes substantially higher strain hardening at mean strain values close to 0, reaching higher peak stresses. Difference in strain hardening can be observed in the evolution of CRSS and total slip in Figures 8b and c, as the loading with lower mean strain generates more plastic slip, which in turn elevates the average CRSS more significantly. The variation in strain hardening behavior ultimately results in the peak stress evolution shown in Figure 8a. The effect of mean strain on the peak stress becomes noticeable as early as the end of the first cycle (Fig. 7a), where the simulation with the lowest mean strain achieves the highest axial stress. This trend is maintained throughout the cyclic loading as the difference between responses evolves into an even more significant gap. It has to be stated, however, that the evolution of peak stress alone may not always describe the change in material behavior completely. During the simulation with the highest mean strain (0.4%), the change in the peak stress is very limited, as shown in Figure 8a. In contrast, the hysteresis loop gets narrower as the cycling progresses, comparing the hysteresis loops for 0.4% mean strain shown in Figures 7a and b.

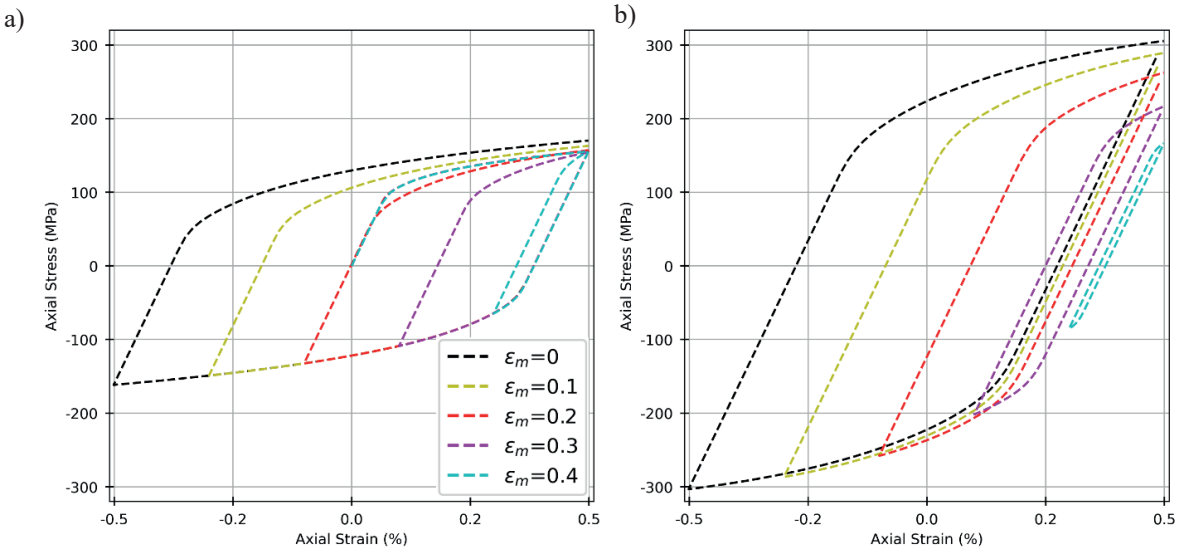

Fig. 7. Hysteresis loops for 1st (a) and 70th (b) cycles obtained by simulations under cyclic loading with 0.5% maximum strain and varying mean strain (ε_m)

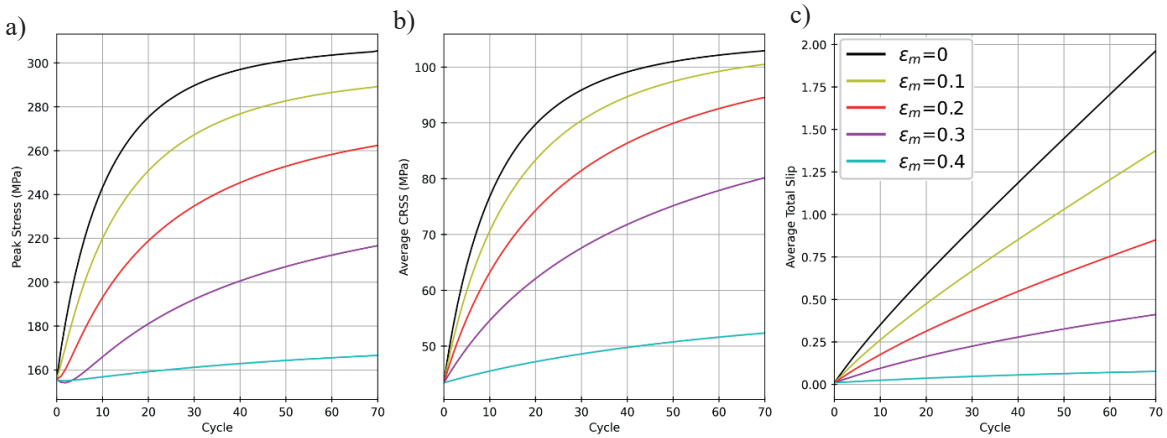

Fig. 8. Evolution of peak axial true stress (a), average CRSS (b), and average total slip (c) under cyclic loading with 0.5% maximum strain and varying mean strain (ε_m)

Additional simulations were performed to investigate stress relaxation behavior under cyclic loading with hold periods (CLH). The symmetric strain-controlled loading with a 0.5% strain amplitude was modified to incorporate 3-minute hold periods at the tensile peak of each cycle. Hysteresis loops for the 1st and 70th cycles are shown in Figure 9. The material response during unloading from compression and loading in tension remains similar to that observed in the CL case. However, due to stress relaxation during the hold period, unloading from tension begins from a reduced stress level, leading to visible modifications in the unloading from tension and subsequently loading in compression phases of the hysteresis loops.

Figure 10 shows the peak stress evolution under CLH loading. In contrast to the experimental results reported by Du et al. (2023), where cyclic holds caused an 18 MPa decrease in saturated peak stress, the simulations predict no significant change in peak stress due to hold periods. Despite minor changes in loop shape, the similarity of the 70th cycle hysteresis loops and peak stress trends between CL and CLH loadings indicates that the current model does not capture the experimentally observed decrease in saturated stress and softer mechanical response under CLH conditions. A more physically motivated crystal plasticity model that explicitly accounts for dislocation generation and annihilation mechanisms may be required to reproduce this behavior.

The evolution of the magnitude of stress relaxation is illustrated in Figure 11a, showing that the amount of decrease in macroscopic stress during strain-holds increases throughout loading. Stress relaxation magnitude eventually saturates at the end of the simulation at the value of 32 MPa. Figure 11b presents the stress relaxation behavior during the hold periods of the 5th and 70th CLH cycles as a function of the hold time. Both the simulation and the experiment exhibit a two-stage relaxation response: an initial rapid stress drop followed by a slower, nearly linear decrease. In the 5th cycle, the simulation predicts a steeper initial decline compared to the experiment, while the relaxation rates in the second stage are in close agreement. By the 70th cycle, where peak stress and stress relaxation magnitude have stabilized, the simulation accurately reproduces the time-dependent relaxation behavior in both magnitude and shape.

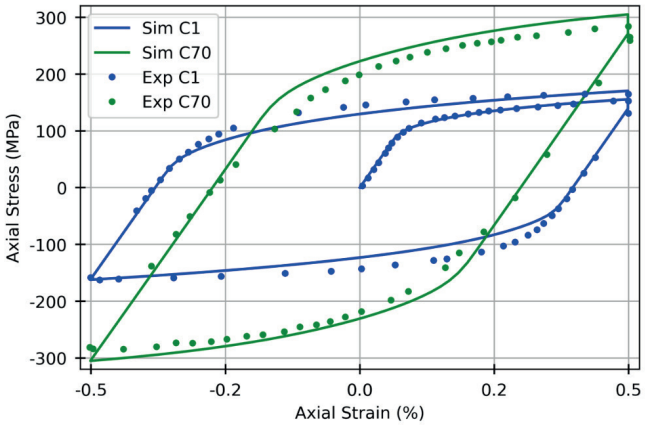

Fig. 9. Hysteresis loops for 1st and 70th cycles obtained by experiments taken from work by Du et al. (2023) and simulations under symmetric loading with 0.5% strain amplitude and 3-minute cyclic strain-holds

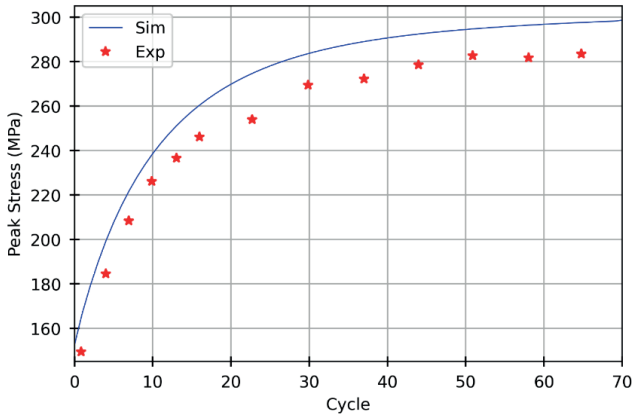

Fig. 10. Evolution of the peak stress obtained by simulation and experiment taken from work by Du et al. (2023) under symmetric cyclic loading with 0.5% strain amplitude and 3-minute strain-holds

Beyond the macroscopic response, the spatial distribution of axial stress across the microstructure is analyzed to assess local variations. At each time step, axial stress values within the RVE are grouped into 10 MPa intervals, and their normalized frequency is plotted to track the evolution of stress distribution. Figure 12 presents these frequency distributions before and after the strain-hold periods of the 1st and 70th cycles. The narrower distribution in the 1st cycle, with a more pronounced frequency peak, indicates a relatively uniform mechanical response at the early stages of loading. As cycling progresses, regions initially carrying higher stress undergo greater strain hardening, resulting in a broader spread in stress values by the 70th cycle, and a flatter frequency profile. This reflects an increasing difference between the mechanical responses of soft and hard regions within the microstructure. Comparing the frequency distributions before and after the hold periods, a near-uniform leftward shift along the stress axis is observed for hold periods of both the 1st and the 70th cycles, suggesting that stress relaxation occurs broadly across the microstructure rather than being confined to isolated hotspots. This observation is further supported by the axial true stress contours shown in Figure 13, which illustrate that stress relaxation during the hold period of the 70th cycle takes place throughout the domain, not just in localized regions.

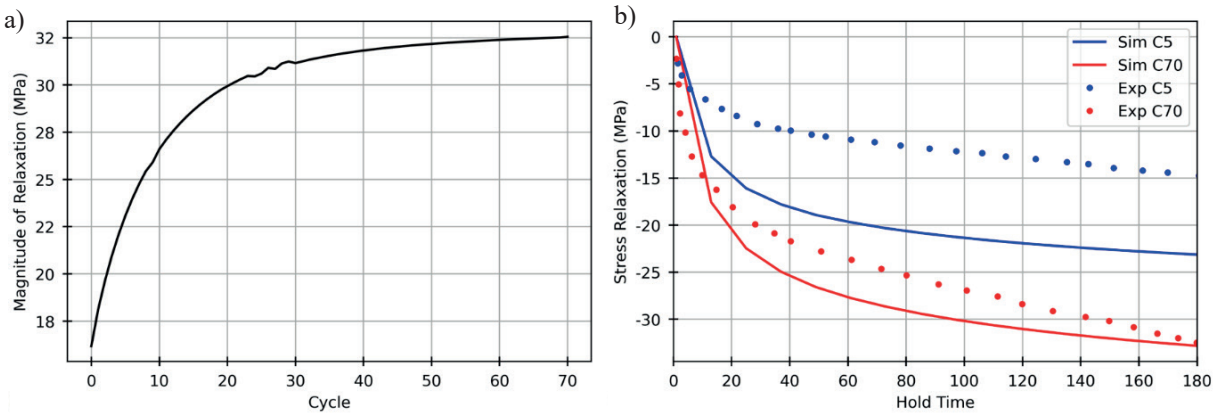

Fig. 11. Evolution of stress relaxation magnitude (a) and stress relaxation behavior (b) during the hold phase of 5th and 70th cycles obtained by simulation and experiment taken from work by Du et al. (2023) under symmetric cyclic loading with 0.5% strain amplitude and 3-minute strain-holds

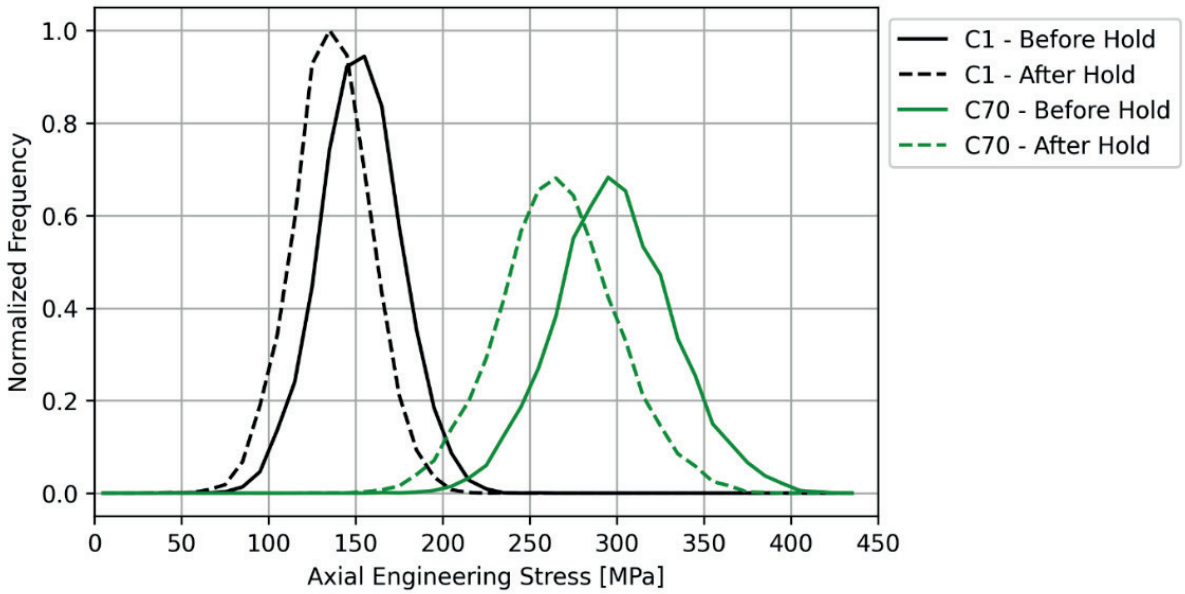

Fig. 12. Normalized frequency of axial stress values across the microstructure grouped into 10 MPa intervals before and after the strain-hold period of the 1st and 70th cycles

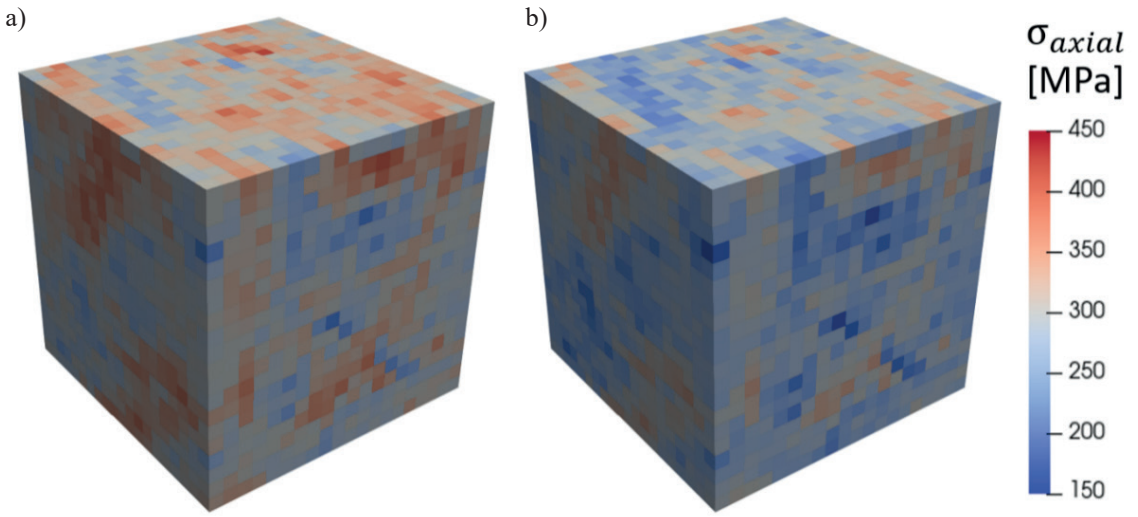

Fig. 13. Spatial distribution of axial true stress in the polycrystalline RVE before (a) and after (b) the hold phase of the 70th cycle under symmetric loading with 0.5% strain amplitude and 3-minute strain-holds

5. Conclusions

This study presents an investigation of the cyclic plasticity and stress relaxation behavior of 316H austenitic stainless steel at elevated temperatures using the DAMASK framework. A combined isotropic–kinematic hardening crystal plasticity model is calibrated against experimental hysteresis loops to capture the low-cycle fatigue response under strain-controlled loading at 550°C. The same model is employed to predict material behavior under cyclic loading with 3-minute hold periods applied at peak strain. Simulation results show strong agreement with experimental data in predicting the evolution of peak stress during symmetric cycling without hold periods. Local variations in mechanical response across the microstructure are captured, driven by differences in crystallographic orientation and grain interactions. Simulations with varying mean strain showed that loading with low mean strain leads to compressive plasticity, which results in additional plastic slip accumulation, and amplification of CRSS and peak stress. Under loading with hold periods, the model reproduces the characteristic two-stage stress relaxation behavior observed experimentally: an initial rapid drop followed by a slower, near-linear decline. However, it fails to replicate the reduction in saturated peak stress reported in experiments when hold periods are introduced. This discrepancy suggests that additional physical mechanisms, such as thermally activated recovery or diffusion-assisted climb, may need to be incorporated to fully describe the fatigue–creep interaction in 316H at reactor-relevant temperatures. Future work may focus on extending the constitutive model to better account for such time-dependent recovery processes.

References

Acar, S. S., & Yalçinkaya, T. (2025a). Crystal plasticity modelling of time-dependent strain accumulation of stainless steel at room temperature. *Philosophical Magazine*, 1–21. https://doi.org/10.1080/14786435.2025.2536601

Acar, S. S., & Yalçinkaya, T. (2025b). Modeling of the stress path-dependent strain ratcheting behaviour of 304L stainless steel through crystal plasticity frameworks. *Metals and Materials International*, *31*(9), 2525–2540. https://doi.org/10.1007/s12540-025-01907-w

Acar, S. S., Bulut, O., & Yalçinkaya, T. (2022). Crystal plasticity modeling of additively manufactured metallic microstructures. *Procedia Structural Integrity*, *35*, 219–227. https://doi.org/10.1016/j.prostr.2021.12.068

AFCEN – Association Francaise pour les Regles de Conception et de Construction des Materiels des Chaudieres Electro-Nucleaires (1985). *Design and Construction Rules for Mechanical components of FBR islands: RCC-MR* (t. 1, vol. Z: *Technical appendix A3*).

Agius, D., Al Mamun, A., Simpson, C. A., Truman, C., Wang, Y., Mostafavi, M., & Knowles, D. (2020). Microstructure-informed, predictive crystal plasticity finite element model of fatigue-dwells. *Computational Materials Science*, *183*, 109823. https://doi.org/10.1016/j.commatsci.2020.109823

Allen, C., Coules, H., Truman, C. E., Mokhtarishirazabad, M., McKendrey, S., Billings, A., Liu, C., Davies, C. M., & Kelleher, J. (2025). Prediction of multiaxial deformation of 316H stainless steel at high temperature using a multiscale crystal plasticity approach. *Materials Science and Engineering: A*, *931*, 148160. https://doi.org/10.1016/j.msea.2025.148160

Aydiner, I. U., Tatli, B., & Yalçinkaya, T. (2024). Investigation of failure mechanisms in dual-phase steels through cohesive zone modeling and crystal plasticity frameworks. *International Journal of Plasticity*, *174*, 103898. https://doi.org/10.1016/j.ijplas.2024.103898

Chen, B., Smith, D. J., Flewitt, P. E. J., & Spindler, M. W. (2011). Constitutive equations that describe creep stress relaxation for 316H stainless steel at 550°C. *Materials at High Temperatures*, *28*(3), 155–164. https://doi.org/10.3184/096034011X13119593388654

Coules, H. E., Nneji, S. O., James, J. A., Kabra, S., Hu, J. N., & Wang, Y. (2022). Full-tensor Measurement of Multiaxial Creep Stress Relaxation in Type 316H Stainless Steel. *Experimental Mechanics*, *62*(1), 19–33. https://doi.org/10.1007/s11340-021-00755-0

Geus, T. W. J., de, Vondřejc, J., Zeman, J., Peerlings, R. H. J., & Geers, M. G. D. (2017). Finite strain FFT-based non-linear solvers made simple. *Computer Methods in Applied Mechanics and Engineering*, *318*, 412–430. https://doi.org/10.1016/j.cma.2016.12.032

Du, R., Song, H., Gao, F., Mo, Y., Yan, Z., Zhuang, Z., Liu, X., & Wei, Y. (2023). Machine learning informed visco-plastic model for the cyclic relaxation of 316H stainless steel at 550° C. *International Journal of Plasticity*, *170*, 103743. https://doi.org/10.1016/j.ijplas.2023.103743

Eisenlohr, P., Diehl, M., Lebensohn, R. A., & Roters, F. (2013). A spectral method solution to crystal elasto-viscoplasticity at finite strains. *International Journal of Plasticity*, *46*, 37–53. https://doi.org/10.1016/j.ijplas.2012.09.012

Erinosho, T. O., Abburi Venkata, K., Mostafavi, M., Knowles, D. M., & Truman, C. E. (2018). Influence of prior cyclic plasticity on creep deformation using crystal plasticity modelling. *International Journal of Solids and Structures*, *139–140*, 129–137. https://doi.org/10.1016/j.ijsolstr.2018.01.028

Gredis, A. (2022). *Environmental effects on the integrity of type 316H stainless steel of an AGR coolant* [Doctor's thesis, University of Manchester]. National Archive of PhD Theses. https://doi.org/10.12681/eadd/54604

Hormozi, R., Biglari, F., & Nikbin, K. (2015). Experimental study of type 316 stainless steel failure under LCF/TMF loading conditions. *International Journal of Fatigue*, *75*, 153–169. https://doi.org/10.1016/j.ijfatigue.2015.02.014

Hu, C., Xu, L., Zhao, L., Han, Y., Song, K., Luo, X., & Li, C. (2023). Investigation of low cycle fatigue crack propagation behavior of 316H steel at 550℃ based on cyclic response and damage accumulation: experiment and modelling. *International Journal of Plasticity*, *167*, 103661. https://doi.org/10.1016/j.ijplas.2023.103661

Hu, J., & Cocks, A. C. F. (2016). A multi-scale self-consistent model describing the lattice deformation in austenitic stainless steels. *International Journal of Solids and Structures*, *78–79*, 21–37. https://doi.org/10.1016/j.ijsolstr.2015.09.021

Hughes, D. G. J., Chevalier, M., & Dean, D. W. (2019). Recent developments in the R5 procedures for assessing the high temperature response of structures. In *ASME 2019 Pressure Vessels & Piping Conference* (vol. 6A: *Materials and Fabrication*). https://doi.org/10.1115/PVP2019-93838

Karjalainen, L. P., & Perttula, J. (1996). Characteristics of static and metadynamic recrystallization and strain accumulation in hot-deformed austenite as revealed by the stress relaxation method. *ISIJ International*, *36*(6), 729–736. https://doi.org/10.2355/isijinternational.36.729

Nasser, M., Davies, C. M., & Nikbin, K. (2016). The influence of AGR gas carburisation on the creep and fracture properties of type 316H stainless steel. In *ASME 2016 Pressure Vessels and Piping Conference* (vol. 5: *High-Pressure Technology*). https://doi.org/10.1115/PVP2016-63076

Pan, Z., Li, Y., Song, Y., Shen, R., Xie, Y., Jin, W., Zhang, K., & Gao, Z. (2022). Effects of strain rate on the tensile and creep-fatigue properties of 316H stainless steel. *International Journal of Pressure Vessels and Piping*, *200*, 104774. https://doi.org/10.1016/j.ijpvp.2022.104774

Petkov, M. P., Hu, J., & Cocks, A. C. F. (2019). Self-consistent modelling of cyclic loading and relaxation in austenitic 316H stainless steel. *Philosophical Magazine*, *99*(7), 789–834. https://doi.org/10.1080/14786435.2018.1556407

Petkov, M. P., Chevalier, M., Dean, D., & Cocks, A. C. F. (2021). Creep-fatigue interactions in type 316H under typical high-temperature power plant operating conditions. *International Journal of Pressure Vessels and Piping*, *194*(B), 104500. https://doi.org/10.1016/j.ijpvp.2021.104500

Phan, V.-T., Messner, M. C., & Sham, T.-L. (2019). A unified engineering inelastic model for 316H stainless steel. In *ASME 2019 Pressure Vessels and Piping Conference* (vol. 1: *Codes and Standards*). https://doi.org/10.1115/PVP2019-93641

Quey, R., Dawson, P. R., & Barbe, F. (2011). Large-scale 3D random polycrystals for the finite element method: Generation, meshing and remeshing. *Computer Methods in Applied Mechanics and Engineering*, *200*(17–20), 1729–1745. https://doi.org/10.1016/j.cma.2011.01.002

Roters, F., Eisenlohr, P., Kords, C., Tjahjanto, D. D., Diehl, M., & Raabe, D. (2012). DAMASK: the Düsseldorf Advanced MAterial Simulation Kit for studying crystal plasticity using an FE based or a spectral numerical solver. *Procedia IUTAM*, *3*, 3–10. https://doi.org/10.1016/j.piutam.2012.03.001

Roters, F., Diehl, M., Shanthraj, P., Eisenlohr, P., Reuber, C., Wong, S. L., Maiti, T., Ebrahimi, A., Hochrainer, T., Fabritius, H.-O., Nikolov, S., Friák, M., Fujita, N., Grilli, N., Janssens, K. G. F., Jia, N., Kok, P. J. J., Ma, D., Meier, F., … Raabe, D. (2019). DAMASK – The Düsseldorf Advanced Material Simulation Kit for modeling multi-physics crystal plasticity, thermal, and damage phenomena from the single crystal up to the component scale. *Computational Materials Science*, *158*, 420–478. https://doi.org/10.1016/j.commatsci.2018.04.030

Shanthraj, P., Eisenlohr, P., Diehl, M., & Roters, F. (2015). Numerically robust spectral methods for crystal plasticity simulations of heterogeneous materials. *International Journal of Plasticity*, *66*, 31–45. https://doi.org/10.1016/j.ijplas.2014.02.006

Tatli, B., & Yalçinkaya, T. (2025). Modelling of Hydrogen-Induced Failure in Polycrystalline Materials through a Strain Gradient Crystal Plasticity Framework. *Procedia Structural Integrity*, *68*, 1140–1146. https://doi.org/10.1016/j.prostr.2025.06.179

Wang, H., Clausen, B., Tomé, C. N., & Wu, P. D. (2013). Studying the effect of stress relaxation and creep on lattice strain evolution of stainless steel under tension. *Acta Materialia*, *61*(4), 1179–1188. https://doi.org/10.1016/j.actamat.2012.10.027

Wang, Y. Q., Spindler, M. W., Truman, C. E., & Smith, D. J. (2016). Critical analysis of the prediction of stress relaxation from forward creep of Type 316H austenitic stainless steel. *Materials & Design*, *95*, 656–668. https://doi.org/10.1016/j.matdes.2016.01.118

Wollmershauser, J. A., Clausen, B., & Agnew, S. R. (2012). A slip system-based kinematic hardening model application to in situ neutron diffraction of cyclic deformation of austenitic stainless steel. *International Journal of Fatigue*, *36*(1), 181–193. https://doi.org/10.1016/j.ijfatigue.2011.07.008

Xu, L., Bao, F., Zhao, L., Han, Y., Jing, H., Yu, H., & Gong, X. (2021). Characterizing microstructural evolution and low cycle fatigue behavior of 316H austenitic steel at high-temperatures. *Journal of Nuclear Materials*, *546*, 152758. https://doi.org/10.1016/j.jnucmat.2020.152758

Xu, L., Li, C., Zhao, L., Han, Y., & Hao, K. (2022). Investigation on the creep-fatigue crack growth behavior of 316H welded joints in sodium-cooled fast reactors. *Engineering Failure Analysis*, *141*, 106684. https://doi.org/10.1016/j.engfailanal.2022.106684

Yalçinkaya, T., Çakmak, S. O., & Tekoğlu, C. (2021). A crystal plasticity based finite element framework for RVE calculations of two-phase materials: Void nucleation in dual-phase steels. *Finite Elements in Analysis and Design*, *187*, 103510. https://doi.org/10.1016/j.finel.2020.103510

Zhao, Z., & Chen, X. (2020). Effect of cyclic softening and stress relaxation on fatigue behavior of 2.25Cr1Mo0.25V steel under strain-controlled fatigue-creep interaction at 728 K. *International Journal of Fatigue*, *140*, 105848. https://doi.org/10.1016/j.ijfatigue.2020.105848